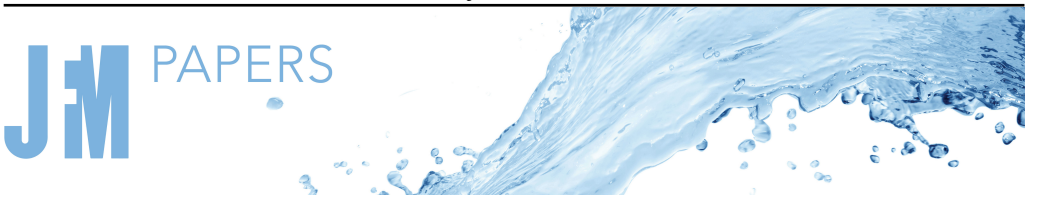
J. Fluid Mech. (2026), *vol.* 1045, A15, doi:10.1017/jfm.2026.12120



Controlling turbulent wall flows via composite active excitations

Yong Ji[1,2], **Peng-Yu Duan**[2], **Jie Yao**[3], **Philipp Schlatter**[4] **and Xi Chen**[2]

[1]School of Mathematics and Statistics, Ningxia University, Yinchuan 750021, PR China

[2]Key Laboratory of Fluid Mechanics of Ministry of Education, Beihang University (Beijing University of Aeronautics and Astronautics), Beijing 100191, PR China

[3]School of Interdisciplinary Science, Beijing Institute of Technology, Beijing 100081, PR China

[4]Institute of Fluid Mechanics (LSTM), Friedrich–Alexander–Universität (FAU) Erlangen–Nürnberg, Erlangen 91058, Germany

Corresponding author: Xi Chen, chenxi97@outlook.com

(Received 27 January 2026 UTC; revised 15 July 2026 UTC; accepted 14 August 2026 UTC)

A sustained drag reduction rate $R > 28\,\%$ (with net power saving $> 26\,\%$) is obtained for turbulent channels at a series of Reynolds numbers (i.e. $Re_\tau = 180,\ 395,\ 550$) via a composite drag control (CDC). This strategy combines opposition control (OC) and large-scale spanwise opposed wall-jet forcing (SOJF), enabling superior suppression of drag-producing near-wall turbulent structures. Parameter searching over 114 simulations is conducted here, and the maximum drag reduction obtained from CDC is much higher than that produced by either SOJF (e.g. $14\,\%$ at $Re_\tau = 550$) or OC (e.g. $20\,\%$ at $Re_\tau = 550$). Flow analysis shows that CDC is more effective in suppressing random turbulence than OC, and it further weakens the secondary flows between colliding motions of SOJF. Interestingly, the pre-multiplied spectrum of the wall shear stress fluctuation (τ_w') under CDC exhibits an unanticipated sharp peak at $k_x^+ \approx 0.026$ for all Reynolds numbers considered here, and τ_w' displays streamwise periodic belts that are absent under OC and SOJF. These belts are found to be induced by wall-normal motion that exhibits the same streamwise periodicity at the length scale of $\lambda_x^+ \approx 240$. Through proper orthogonal decomposition, the belt structures are confirmed in the first three modes of fluctuating velocity fields, and the dynamic period is found to be $T^+ \approx 30$ in viscous time scale. Finally, vortical decomposition suggests that eliminating the turbulent vortical dispersion in the wall-normal direction should be the target for enhancing the efficacy of CDC at even higher Reynolds numbers.

Key words: boundary layer control, boundary layer structure, drag reduction

© The Author(s), 2026. Published by Cambridge University Press.

https://doi.org/10.1017/jfm.2026.12120 Published online by Cambridge University Press

1. Introduction

Reducing the skin-friction drag in wall turbulence is of great importance in improving the speed and fuel efficiency of aeroplanes, underwater vehicles and many other means of transportation. To reduce drag, numerous control strategies have been studied (Corke & Thomas 2018; Chung *et al.* 2021; Ricco *et al.* 2021; Fukagata *et al.* 2024). Control methods that do not require any input energy are usually implemented by changing the surface condition, which adjusts the turbulence structure near the wall, such as through riblets (Choi *et al.* 1993; Bechert *et al.* 1997; Gatti *et al.* 2020; Modesti *et al.* 2021), superhydrophobic surfaces (Rothstein 2010; Checco *et al.* 2014; Park *et al.* 2014; Rastegari & Akhavan 2018) and roughness elements (Jimenez 2004; Chung *et al.* 2021). In the case of riblets, tiny sizes are required for drag reduction, which means that they are easily eroded by atmospheric dust (Ricco *et al.* 2021). For superhydrophobic surfaces, drag reductions of up to 50 % for the turbulent channel (Rothstein 2010) and 75 % for the turbulent boundary layer (Park *et al.* 2014) are obtained in laboratories, but a high shear rate or pressure can easily destroy superhydrophobic surfaces (Checco *et al.* 2014; Rastegari & Akhavan 2018). These issues limit the practical application of passive surface control.

When an external excitation is introduced, the self-sustaining cycle of near-wall vortices is expected to break and hence lead to drag reduction (Kim & Bewley 2007; Chung & Talha 2011; Deng & Xu 2012; Mamori *et al.* 2014). Typical operations include wall oscillations and streamwise travelling waves (Jung *et al.* 1992; Quadrio *et al.* 2009; Agostini *et al.* 2014; Yakeno *et al.* 2014; Chandran *et al.* 2023; Deshpande *et al.* 2023; Rouhi *et al.* 2023) and blowing/suction control (Choi *et al.* 1994; Sumitani & Kasagi 1995; Kametani & Fukagata 2011; Guseva & Jiménez 2022). For travelling-wave methods, a wide range of parameter searches have been performed to explore the optimal drag reduction when the Reynolds number (Re) changes, and a prediction for a high-drag-reduction Re has been given based on scaling models (Hurst *et al.* 2014; Gatti & Quadrio 2016). For blowing and suction control, imposing a specific wall velocity to counteract the sweep and ejection effects produced by streamwise vortices in the buffer layer can reduce drag by 25 % at moderate friction Reynolds numbers of $Re_\tau = 110$–180 (Choi *et al.* 1994; Deng *et al.* 2014). As it is difficult to determine the appropriate wall velocity in the buffer layer in real-time control, Park & Choi (2020) developed convolutional neural networks to construct a map between the appropriate wall velocity and various wall parameters. Subsequent work in this direction by Han & Huang (2020) resulted in drag reduction of 15 % for $Re_\tau = 390$–580.

In numerical studies, flow control is excited by applying a body force (Ricco *et al.* 2021) in the Navier–Stokes equations. Schoppa & Hussain (1998) added body forces to the Fourier space to induce counter-rotating streamwise swirls in channels at $Re_\tau = 100$. Later, counter-rotating swirls at higher Re were employed by Canton *et al.* (2016) and Yao *et al.* (2018), and a 15 % drag reduction was obtained at $Re_\tau = 550$ by adjusting the wall-normal location of the controlling swirls. A series of numerical studies by Schoppa & Hussain (1998), Canton *et al.* (2016) and Yao *et al.* (2018) inspired experimental investigations using synthetic wall jets (Iuso *et al.* 2002; Cannata *et al.* 2020) and plasma actuation (Thomas *et al.* 2016; Cheng *et al.* 2021; Duong *et al.* 2021). Recently, large-scale control strategies on rough walls have been investigated by Duan *et al.* (2024) and Nozarian *et al.* (2024), and robust drag reduction has been achieved at the moderate value of $Re_\tau = 180$.

As Re increases, large-scale outer movements contribute more to skin friction (de Giovanetti *et al.* 2016). An experimental study on the control of these structures (Marusic *et al.* 2021) reported a significant 13 % drag reduction and 10 % net power saving at

https://doi.org/10.1017/jfm.2026.12120 Published online by Cambridge University Press

$Re_\tau = 12\,800$. In these experiments, the spanwise wall oscillation frequency was lowered to produce the effective suppression of flow structures with relatively large wavelengths, resulting in notable drag reduction for a small energy input. The idea of large-scale wall opposition control has been applied at $Re_\tau = 932$ to enhance the intensity or mixing of turbulence (Guseva & Jiménez 2022). Recently, direct numerical simulations (DNS) of spanwise wall oscillations have been extended to high Reynolds numbers. Xiao *et al.* (2024) conducted a DNS study of rotating pipes with Re_τ up to 3000, and observed the suppression of large-scale motions associated with a very high drag reduction. For rough walls, Deshpande *et al.* (2024) showed that spanwise wall oscillations can yield drag reduction of up to 25 %. However, in open channels, the DNS conducted by Gatti *et al.* (2025) for $Re_\tau \approx 6000$ suggested that the drag reduction rate decreases with increasing Re, regardless of the control parameters of the spanwise wall oscillations.

In addition to numerical and laboratory experiments, several theoretical frameworks have been developed in which the drag coefficient is represented through volume integration of different mean quantities. Using the mean momentum equation, the Fukagata–Iwamoto–Kasagi (FIK) identity (Fukagata *et al.* 2002) was obtained and used to analyse the drag contributions of (equivalent) laminar and turbulent motions (Yudhistira & Skote 2011; de Giovanetti *et al.* 2016; Yoon *et al.* 2016). Floryan (2023) further argued that the laminarisation of the flow results in a limit for the potential drag reduction in turbulent channels. In view of energy dynamics, Renard & Deck (2016) decomposed C_f into the integral of the mean flow dissipation and turbulent production; this formulation has been extended to compressible flows (Li *et al.* 2019) and rough walls (Zhang *et al.* 2024). Analysis of the energy flux introduced by Gatti *et al.* (2018) led to a dissipation-based expression for C_f (Chen *et al.* 2021). Roccon *et al.* (2021) used a similar framework to analyse drag reduction in turbulent lubricated channel flows. Recently, Zhao *et al.* (2024) proposed a drag decomposition based on velocity–vorticity correlations, and investigated the physical relations between the generation of wall friction and vortical motions.

Despite the studies mentioned above, there is still a gap between academic research and practical applications. A major difficulty lies in the decreasing efficacy of drag reduction at high Re (Corke & Thomas 2018; Ricco *et al.* 2021). While different strategies have their own character, combining the merits of different strategies together appears to be a new direction. The current work aims to verify the efficacy of composite drag control (CDC) by combining the active excitations of opposition flows and large-scale swirls. The underlying mechanism is that large-scale swirls merge near-wall streaks and suppress the generation of streamwise vortices (Waleffe 1997; Jiménez & Pinelli 1999), and the secondary flows between the colliding motions could be further inhibited by blowing and suction, resulting in a greater reduction in drag. This idea was tested in our preliminary study but only at a single Reynolds number of $Re_\tau \approx 200$ (Yao *et al.* 2021). In this study, we performed a wider search for parameters and considered the Re_τ trend of drag reduction at $Re_\tau = 180$, 395 and 550. Interestingly, we find a significant and robust drag reduction of more than 28 % for all Reynolds numbers, demonstrating the potential of additive and synergistic control methods. The results thus offer a composite perspective for the development of effective drag controls.

The paper is organised as follows. The numerical scheme and control methods are presented in § 2. Mean flow statistics and coherent structures are examined in § 3 to elucidate the underlying physics of drag control. Section 4 introduces the spectrum analysis and proper orthogonal decomposition (POD), while § 5 is devoted to the vortical decomposition of skin friction. The concluding remarks are given in § 6.

https://doi.org/10.1017/jfm.2026.12120 Published online by Cambridge University Press

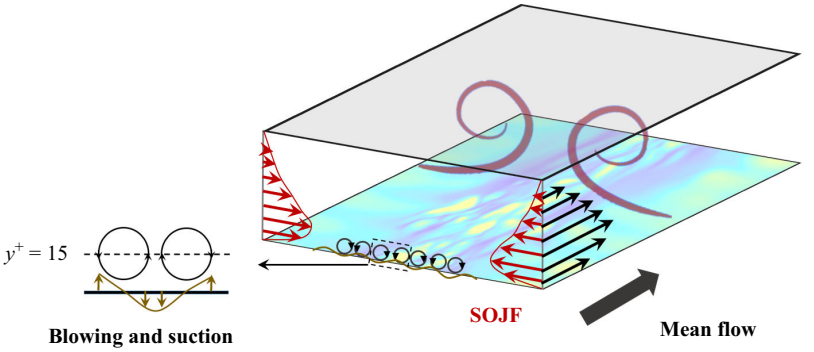


Figure 1. Schematic for CDC, which combines SOJF and OC. Note that SOJF generates large-scale swirls which transport velocity streaks (blue contours) into the middle span and merges them together; OC further weakens the streak envelopes via surface blowing and suction.

2. Computational set-up

2.1. *Control schemes*

The governing equations for incompressible turbulent channel flow are the Navier–Stokes equations:

$$\partial_i u_i = 0, \tag{2.1}$$

$$\partial_t u_i + \partial_j u_i u_j = \nu \partial_j \partial_j u_i - \partial_i p/\rho + F_i, \tag{2.2}$$

where the subscript i denotes the direction (x, y, z) in Cartesian coordinates; u_i is the corresponding velocity in the streamwise, wall-normal and spanwise directions; ν is the fluid kinematic viscosity; p is the pressure; ρ is the density; and F_i is the external volume force. Following previous studies (Yao *et al.* 2018; Ricco *et al.* 2021), the volume force, referred to as the spanwise opposed wall-jet force, is set as

$$F_x = F_y = 0; \quad F_z = A_s \sin(\beta z) g(y), \tag{2.3}$$

where A_s is the forcing amplitude; β $(= 2\pi/\lambda)$ is the spanwise wavenumber; and $g(y)$ is a dimensionless function. In this paper, the friction velocity and viscous length of uncontrolled flow (indicated by subscript 0) are used to non-dimensionalise all control parameters: (*a*) $A_s^+ = A_s \nu/u_{\tau,0}^3$; (*b*) $\lambda^+ = 2\pi/\beta^+$ $(\beta^+ = \beta\nu/u_{\tau,0})$; (*c*) $g(y^+) = y^+ \exp(-\eta y^{+2})$, $y^+ = y u_{\tau,0}/\nu$; where η is the decay factor determining the wall-normal velocity profile of the wall jet. The function g reaches its maximum at $y^+ = y_c^+ = 1/\sqrt{2\eta}$, and its maximum value $y_c^+ \exp(-1/2)$ is used to normalise $g(y)$.

The current work investigates a more efficient control method by combining large-scale spanwise opposed wall-jet forcing (SOJF) with opposition control (OC) (Choi *et al.* 1994; Kametani & Fukagata 2011; Guseva & Jiménez 2022), with the expectation that OC will further eliminate small-scale vortices that escape from the control of SOJF. Therefore, in addition to the forcing in (2.3), the wall-normal velocity at the wall is set as

$$v_w(x, z, t) = -v(x, y_d, z, t), \tag{2.4}$$

where $v(y_d)$ is the wall-normal velocity at the detection plane $y_d^+ = 15$ (hereinafter, the subscript w represents the value on the wall). For compatibility with the forcing in (2.3), such a wall-velocity setting is imposed only on the bottom wall. A sketch of CDC for a channel is shown in figure 1.

https://doi.org/10.1017/jfm.2026.12120 Published online by Cambridge University Press

Case	Re_b	$L_x/h, L_z/h$	$N_x \times N_y \times N_z$	Δy_w^+	Δy_{max}^+	Tu_τ/h	$R\,\%$ ($\delta R\,\%$)	$N\,\%$
CH180	2800	$4\pi, 2\pi$	$192 \times 129 \times 128$	0.05	4.4	42.8	0 (—)	—
OC180	2800	$4\pi, 2\pi$	$192 \times 129 \times 128$	0.05	3.9	37.8	22 (0.7)	21.5
SOJF180	2800	$4\pi, 2\pi$	$192 \times 129 \times 128$	0.05	4.0	38.8	18 (1.1)	15
CDC180	2800	$4\pi, 2\pi$	$192 \times 129 \times 128$	0.04	3.6	34.8	34 (2.0)	33
CH395	6800	$2\pi, \pi$	$256 \times 161 \times 192$	0.07	7.6	52.9	0 (—)	—
OC395	6800	$2\pi, \pi$	$256 \times 161 \times 192$	0.07	6.8	34.0	19 (0.5)	18.6
SOJF395	6800	$2\pi, \pi$	$256 \times 161 \times 192$	0.07	6.9	34.3	18 (0.6)	15
CDC395	6800	$2\pi, \pi$	$256 \times 161 \times 192$	0.06	6.3	31.4	31 (2.3)	29
CH550	10 000	$\pi, 2\pi/3$	$256 \times 193 \times 192$	0.07	8.9	36.5	0 (—)	—
OC550	10 000	$\pi, 2\pi/3$	$256 \times 193 \times 192$	0.07	8.0	32.6	20 (1.4)	19.8
SOJF550	10 000	$\pi, 2\pi/3$	$256 \times 193 \times 192$	0.07	8.2	33.6	16 (1.4)	13
CDC550	10 000	$\pi, 2\pi/3$	$256 \times 193 \times 192$	0.06	7.6	62.2	28 (1.3)	26

Table 1. Details of the numerical discretisation employed in the present simulations, including uncontrolled channel (CH), control with wall oscillations (OC), large-scale swirls (SOJF) and composite excitations (CDC). The numerical discretisation is the same for all CDC cases, and the drag reduction rate R and net power saving N are only given for the optimal control parameters marked in figure 2.

2.2. *Simulation parameters*

The current DNS is conducted using the code of 'Simson' developed by Lundbladh *et al.* (1992), Chevalier *et al.* (2007) and Schlatter *et al.* (2010). The code is based on the spectral integration technique. In the streamwise and spanwise directions, periodic boundary conditions are employed, and in the wall-normal direction, the boundary condition is equation (2.4). Fourier series are adopted for spatial discretisation in the wall-parallel directions, and in the wall-normal direction, Chebyshev series are used. A third-order Runge–Kutta scheme is applied for time integration of the advective and forcing terms. The Crank–Nicolson method for viscous terms is adopted in the streamwise and spanwise directions. By adjusting the mean pressure gradient, the bulk velocity U_b is kept constant. Three bulk Reynolds numbers, i.e. $Re_b = 2800$, 6800 and 10 000, are set to obtain simulations with $Re_\tau = 180$, 395 and 550, respectively. Table 1 lists the domain sizes, spatial resolution and simulation times. The initial condition in all simulations is an uncontrolled, fully developed turbulent velocity field at the same Re_τ.

Drag reduction R is defined as

$$R = (1 - C_f^{control}/C_{f,0}) \times 100\,\%, \tag{2.5}$$

where C_f is evaluated by the friction force (τ_w) at the bottom wall, i.e.

$$C_f/2 = \tau_w/(\rho U_b^2) = U_b^{+2}. \tag{2.6}$$

The uncertainty of R is calculated following the procedure described by Gatti & Quadrio (2016), i.e. $\sigma_R = (C_f/C_{f,0}\sqrt{(\sigma_{C_{f,0}}/C_{f,0})^2 + (\sigma_{C_f}/C_f)^2})$. Here, σ_{C_f} is the standard uncertainty of C_f using an autoregressive method (Oliver *et al.* 2014) and σ_R is the uncertainty of R by propagating the standard uncertainty of C_f. The uncertainty is finally extended to a 95 % confidence interval by $\delta R = 1.96\sigma_R$. The calculated uncertainty of R is listed in table 1.

The net power-saving rate N is defined as

$$N \equiv (1 - (P + P^{in})/P_0) \times 100\,\%, \tag{2.7}$$

https://doi.org/10.1017/jfm.2026.12120 Published online by Cambridge University Press

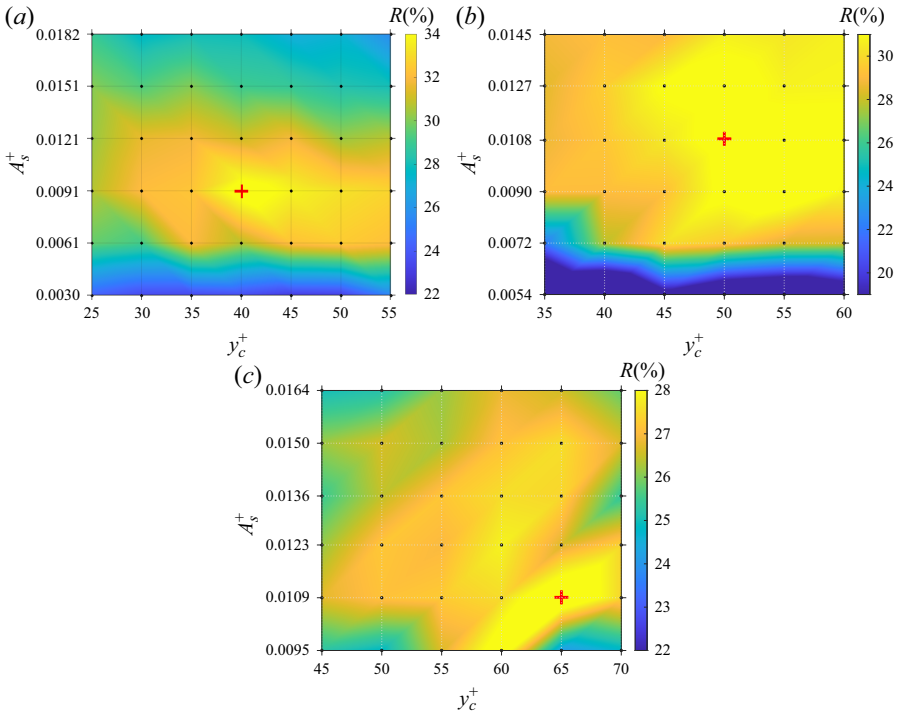


Figure 2. Drag reduction (R) of CDC in the $A_s^+ - y_c^+$ plane for (a) $Re_\tau = 180$, (b) $Re_\tau = 395$ and (c) $Re_\tau = 550$. The symbol • (black) denotes the specific control parameters under CDC. A total of 114 simulations were performed. In each panel, the symbol + (red) denotes the optimal control parameters which yield the largest R for the corresponding Re_τ.

where $P = u_\tau^2 U_b / h$ and $P_0 = u_{\tau,0}^2 U_b / h$ are the total pumping powers of the controlled and uncontrolled channels, respectively, and P^{in} is the input power of the control excitation. In (2.7), the power input is

$$P^{in} = \langle w F_z \rangle + \langle \rho v_w^3 / 2 \rangle + \langle p_w v_w \rangle, \tag{2.8}$$

where $\langle w F_z \rangle$ is the power input corresponding to SOJF (Chen *et al.* 2021) and $\langle \rho v_w^3/2 \rangle + \langle p_w v_w \rangle$ is the energy injected into channel from the wall by OC (Gatti *et al.* 2018). The net power-saving rate N obtained from (2.7) is listed in the last column of table 1.

2.3. *Parameter search*

After adding OC, the optimal forcing amplitude is no longer the same as the value set for SOJF. Thus, a parameter search is performed for each different forcing amplitude and control height. Figures 2(*a*)–2(*c*) show the drag reduction R as a function of A_s^+ and y_c^+ at $Re_\tau = 180$, 395 and 550, respectively. Simulations are carried out at $A_s^+ = [1, 2, 3, 4, 5, 6] \times 0.00303$ and $y_c^+ = [25, 30, 35, 40, 45, 50, 55]$ for $Re_\tau = 180$; $A_s^+ = [3, 4, 5, 6, 7, 8] \times 0.00181$ and $y_c^+ = [35, 40, 45, 50, 55, 60]$ for $Re_\tau = 395$; $A_s^+ = [7, 8, 9, 10, 11, 12] \times 0.00136$ and $y_c^+ = [45, 50, 55, 60, 65, 70]$ for $Re_\tau = 550$. Hence, 114 simulations are performed for CDC, covering a wide range of A_s^+ and y_c^+.

In figure 2, the contours are computed from a linear interpolation of the discrete simulated points. It is impressive that a high value of R can be obtained in broad ranges of the forcing amplitude and the control height. The optimal values of A_s^+ are almost independent of the Reynolds number, i.e. 0.009, 0.011, 0.011 for increasing Re_τ. This

https://doi.org/10.1017/jfm.2026.12120 Published online by Cambridge University Press

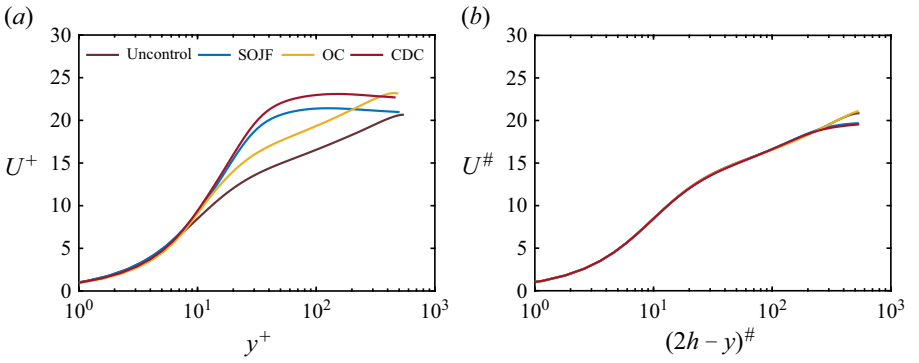


Figure 3. Mean velocity profile along wall-normal direction at $Re_\tau = 550$ for (*a*) the bottom half-channel and (*b*) the top half-channel. The superscripts + and # indicate normalisation by the bottom and top wall-friction velocities, respectively.

suggests a typical velocity of about $4u_\tau$ for the spanwise wall jets, consistent with the plasma experiments conducted by Thomas *et al.* (2016) and Corke & Thomas (2018). Moreover, according to the FIK identity (Fukagata *et al.* 2002), Reynolds shear stress contributes to the turbulent part of C_f, the suppression of which decreases drag. This is consistent with our optimal y_c^+, i.e. 40 for $Re_\tau = 180$, 50 for $Re_\tau = 395$ and 65 for $Re_\tau = 550$, which follows the Re_τ scaling of the Reynolds shear stress peak location (Chen *et al.* 2019). For β, $\lambda^+ = 2\pi/\beta \approx 1200$ under all controls, implying a simultaneous control of 10–12 velocity streaks (because their spanwise spacing is $\lambda_z^+ \approx 100$ (see e.g. Del Alamo & Jimenez 2006)) by a pair of counter-rotating streamwise swirls. Compared with the pure SOJF control, the optimal A_s^+ is slightly smaller under CDC and the optimal y_c^+ is larger. This is because OC weakens the near-wall streaks and shifts the Reynolds shear stress peak outward, as explained later herein.

The maximum drag reduction (R) and the net power saving (N) obtained by CDC at $Re_\tau = 180$ are 34 % and 33 %, respectively (table 1), slightly higher than in our preliminary study (Yao *et al.* 2021). In the Re_τ range considered here, although R decreases with increasing Re_τ, CDC still produces a 28 % drag reduction at $Re_\tau = 550$, much higher than 20 % of OC and 16 % of SOJF. In the following, the optimal control cases are analysed in detail to understand the drag reduction performance.

3. Results of mean flow statistics

3.1. *Mean velocity and Reynolds stresses*

According to (2.6), the volume-integrated mean velocity determines the drag coefficient. Taking $Re_\tau = 550$ as an example, the mean velocity profiles across the bottom half-channel are shown in figure 3(*a*). For OC (yellow line), the logarithmic mean profile is preserved with the same slope as that of uncontrolled flow (black line), but its intercept increases due to a thicker buffer layer (Kametani & Fukagata 2011; Chung *et al.* 2021). In contrast, SOJF (blue line) flattens the mean velocity in the bulk due to the large-scale swirls that homogenise the shear. It is clear that the CDC (red line) resembles the SOJF feature by further lifting the mean profile and therefore yields the smallest C_f. As the velocity changes little for the upper half-channel (figure 3*b*), hereafter we focus on the flow alteration in the lower one.

A common understanding of drag reduction is that turbulent fluctuations must be suppressed, which is reflected in the smaller Reynolds stresses under control (Jeong *et al.*

https://doi.org/10.1017/jfm.2026.12120 Published online by Cambridge University Press

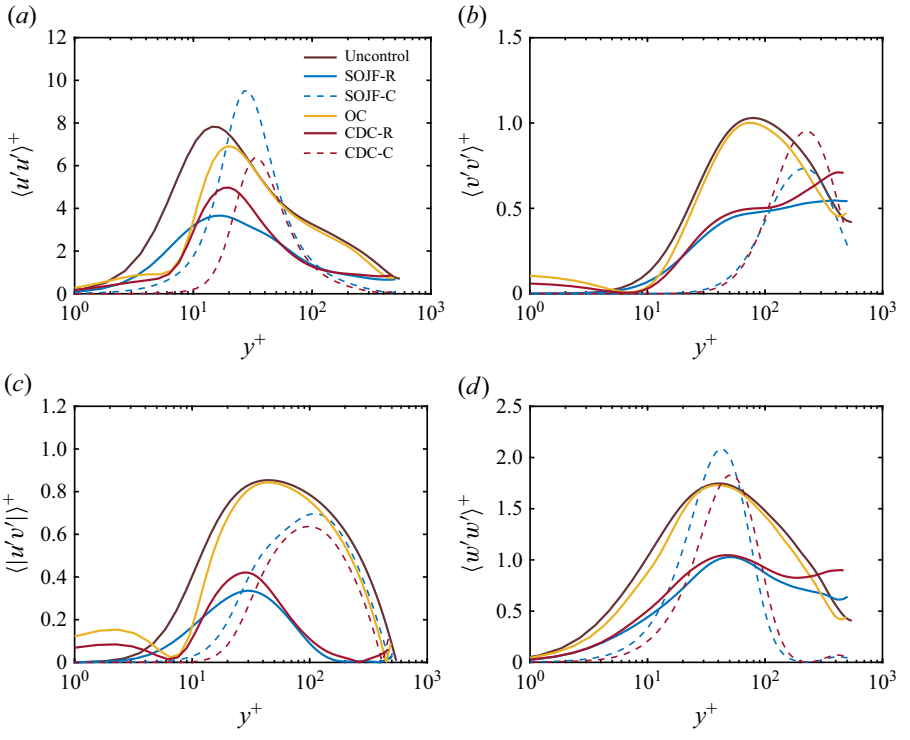


Figure 4. Reynolds stresses under various controls compared with uncontrolled case (black solid line) at $Re_\tau = 550$: (*a*) $\langle u'u'\rangle^+$, (*b*) $\langle v'v'\rangle^+$, (*c*) $\langle |u'v'|\rangle^+$ and (*d*) $\langle w'w'\rangle^+$. Here OC is represented by the yellow solid line. For SOJF (blue) and CDC (red), the solid line corresponds to random fluctuations and the dashed line corresponds to coherent fluctuations.

1997; Jiménez & Pinelli 1999; Guseva & Jiménez 2022). Nevertheless, the current study calls for caution on this point of view, because of the proper Reynolds decomposition needed. For SOJF and CDC, if following the usual Reynolds decomposition by averaging over txz ensembles, the motions of counter-rotating swirls would be mistreated as turbulent fluctuations and lead to larger Reynolds stresses even under significant drag reduction. Therefore, to distinguish random flow motions from coherent large-scale swirls, it is more reasonable to perform a triple decomposition (Chen *et al.* 2021), i.e.

$$u_i = \overline{u}_i + \tilde{u}_i + u'', \quad u_i'' = u_i' - \tilde{u}_i, \tag{3.1}$$

where

$$\tilde{u}_i = \langle u_i \rangle_{xt} - \overline{u}_i. \tag{3.2}$$

Here, the subscript xt indicates averaging the streamwise and time ensembles; $\overline{u}$ is the usual Reynolds-averaged mean velocity; $\tilde{u}$ represents the coherent motions induced by the SOJF in the y–z plane, which are closely associated with the controlling swirls; and u'' is the random turbulent fluctuation. To explain, for flow without control or with OC, u'' is the same as the Reynolds decomposition u' because $\tilde{u}$ is zero and therefore there is no need for trip decomposition.

Using the triple decomposition above, SOJF and CDC induce coherent stresses $\langle \tilde{u}_i \tilde{u}_j \rangle^+$ and random stresses $\langle u_i'' u_j'' \rangle^+$, which are represented by dashed and solid lines, respectively, shown in figure 4. In particular, figure 4(*a*) shows that $\langle u''u'' \rangle^+$ of SOJF or CDC is uniformly lower than $\langle u'u' \rangle^+$ of no control (solid black line). Yet, the sum of

https://doi.org/10.1017/jfm.2026.12120 Published online by Cambridge University Press

$\langle u''u''\rangle^+$ and $\langle \tilde{u}\tilde{u}\rangle^+$, which is the usual Reynolds-averaged stress $\langle u'u'\rangle^+$, is obviously higher than $\langle u'u'\rangle^+$ without control. Similar observations can be made for the other stress components (figure 4*b–d*). Therefore, it is important to exclude coherent motions when highlighting the lower turbulence intensity under drag reduction.

Two notable points for CDC deserve further discussion from figure 4. First, compared with SOJF, coherent motions are weaker under CDC. This is drawn from figure 4(*a*,*c*,*d*), where CDC-C (dashed red line) is lower than SOJF-C (dashed blue line) throughout the flow domain. This conforms to the optimal A_s^+ shown in figure 2, which is smaller for CDC than for SOJF, because A_s^+ represents the strength of coherent swirls. Second, compared with OC, random fluctuations are suppressed under CDC. This is concluded from figure 4 where CDC-R (solid red line) is uniformly lower than OC (solid yellow line). We also observe the effect of the virtual wall under CDC similar to that of OC (Chung & Talha 2011; Deng *et al.* 2014), namely at $y^+ \approx 5$, $\langle v'v'\rangle^+ = 0$ (figure 4*b*) and $\langle |u'v'|\rangle^+ = 0$ (figure 4*c*). From these comparisons, it is well illustrated that CDC combines the advantages of SOJF and OC together, thus generating the largest drag reduction.

To show that near-wall random turbulent structures are suppressed by the large-scale swirls, the pre-multiplied spectra of $k_z\Phi_{uu}(y^+, k_z^+)/u_\tau^2$ and $k_z\Phi_{uv}(y^+, k_z^+)/u_\tau^2$ are shown in figure 5. Without control (figure 5*a*), the maximum of $k_z\Phi_{uu}/u_\tau^2$ is located at $y^+ \approx 15$ and $\lambda_z^+ \approx 100$, where $\lambda_z^+ = 2\pi/k_z^+$ is wavelength. The value $y^+ \approx 15$ corresponds to the inner peak of random $\langle u'u'\rangle^+$ shown in figure 4(*a*), while $\lambda_z^+ \approx 100$ corresponds to the width of the velocity streaks (Schoppa & Hussain 2002; Jimenez & Hoyas 2008). Under CDC (figure 5*c*), the wall-normal location of the spectrum peak shifts outward and the corresponding wavelength becomes $\lambda_z^+ \approx 1000$. Similarly, without control (figure 5*b*), $k_z\Phi_{uv}/u_\tau^2$ has a peak at $y^+ \approx 30$ (Chen *et al.* 2019); under CDC, the peak moves outward to $y^+ \approx 65$ (figure 5*d*). The value of $y^+ \approx 65$ corresponds to the optimal control height y_c^+ in figure 2(*c*), and the wavelength $\lambda_z^+ \approx 1000$ is the spacing between large-scale swirls. A small contour island appears at $y^+ \approx 30$ and $\lambda_z^+ \approx 100$ in figure 5(*d*), implying the contribution of the remnant small-scale streaks to the Reynolds shear stress near the wall. The pre-multiplied spectra of coherent motions, i.e. $k_z\Phi_{\tilde{u}\tilde{u}}/u_\tau^2$ and $k_z\Phi_{\tilde{u}\tilde{v}}/u_\tau^2$, are shown in figures 5(*e*) and 5(*f*), respectively. The near-peak distributions of figures 5(*e*) and 5(*f*) are very similar to those shown in figures 5(*c*) and 5(*d*), except that the small-scale contour islands are absent. This indicates that $\tilde{u}$ and $\tilde{v}$ obtained from the triple decomposition can effectively represent the large-scale coherent swirls.

3.2. *Mean wall shear stress*

Another inspiring way to understand the drag variation is to examine the mean shear stress (after tx-averaging) on the wall, shown in figure 6 for the current three Re_τ values. For OC, $\tau_w/\tau_{w,0}$ is homogeneous along the spanwise direction and plateaus at 0.8; for SOJF, there is a hump in the middle span ($z/L_z = 0.5$) where the magnitude increases moderately with increasing Re_τ; for CDC, the wall shear stress is flattened and has a lower magnitude than under OC, which is around $\tau_w/\tau_{w,0} \approx 0.7$.

To explain why the mid-span hump appears for SOJF and becomes flattened under CDC, figure 7 shows the instantaneous λ_2 vortical structures (Jeong & Hussain 1995), along with the low-speed streaks in the detection plane. For flow without control, numerous slender vortices are generated on top of typical meandering low-speed streaks (figure 7*a*). When OC is applied, the streaks are significantly weakened, and the generation of drag-inducing near-wall streamwise vortices is suppressed, although they are still randomly distributed in the plane (figure 7*b*). Under SOJF, only a single wide meandering streak appears along the mid-span, extending over the entire flow length; the corresponding λ_2 vortices also

https://doi.org/10.1017/jfm.2026.12120 Published online by Cambridge University Press

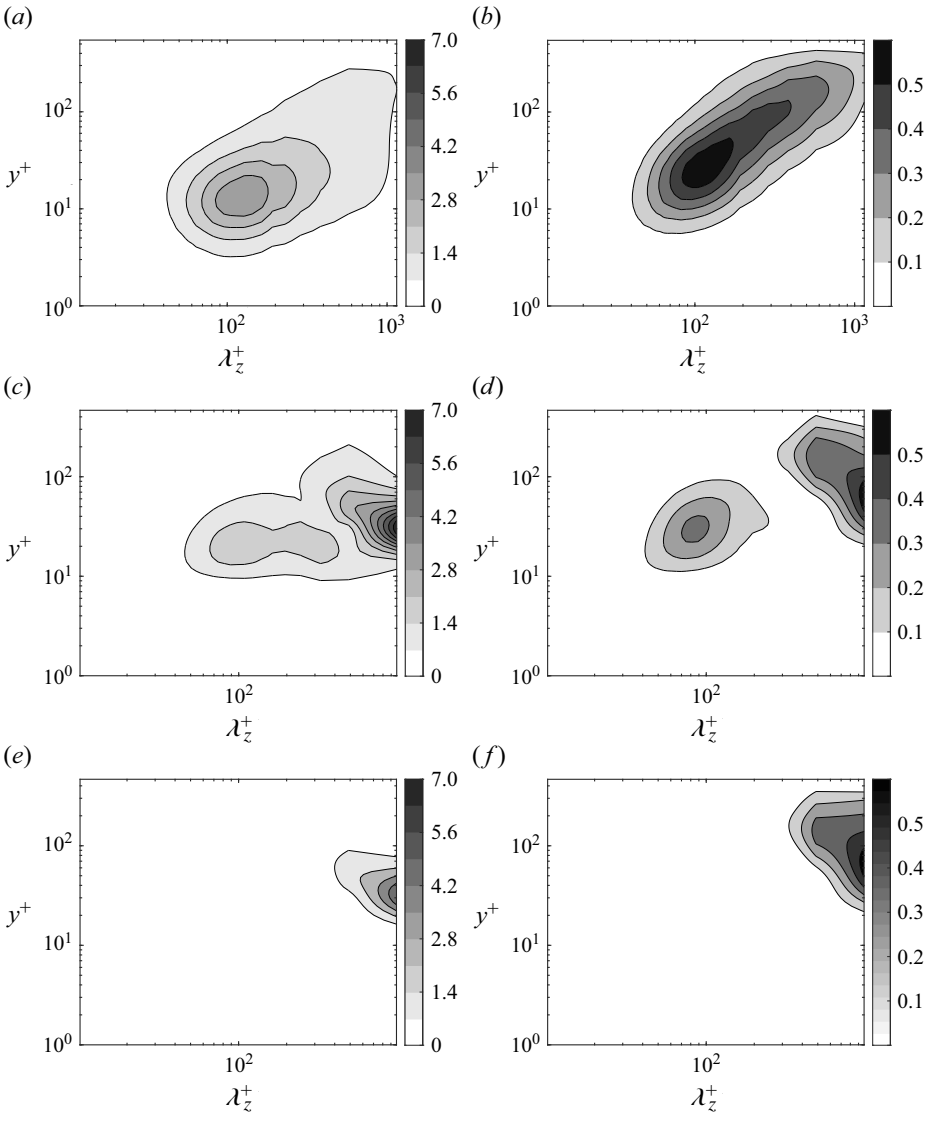


Figure 5. Pre-multiplied spectra of streamwise fluctuation intensity $k_z\Phi_{uu}(y^+, k_z^+)/u_\tau^2$ (*a*,*c*,*e*) and co-spectrum of Reynolds shear stress $k_z\Phi_{uv}(y^+, k_z^+)/u_\tau^2$ (*b*,*d*,*f*): (*a*,*b*) flow without control, (*c*,*d*) flow with CDC, and the coherent $k_z\Phi_{\tilde{u}\tilde{u}}(y^+, k_z^+)/u_\tau^2$ (*e*) and $k_z\Phi_{\tilde{u}\tilde{v}}(y^+, k_z^+)/u_\tau^2$ (*f*) for flow with CDC.

lie along the central collision region, just above the merged streak envelope (figure 7*c*). Therefore, the hump in the wall shear stress in SOJF is induced by the sweeps of secondary flows between the counter-rotating swirls. The additional OC of CDC (figure 7*d*) further eliminates the associated vortical structures, producing the reduced hump along the central region.

A cross-view of the flow is given in figure 8, where the dark colours indicate strong λ_2 structures. Compared with OC (figure 8*b*), the two side regions of the channel are almost laminar under CDC (figure 8*d*); therefore, the random turbulence fluctuations are inhibited. Moreover, compared with SOJF (figure 8*c*), fewer vortices are generated in the mid-span (figure 8*d*) because of the opposite wall-normal motion. Hence, both the number

https://doi.org/10.1017/jfm.2026.12120 Published online by Cambridge University Press

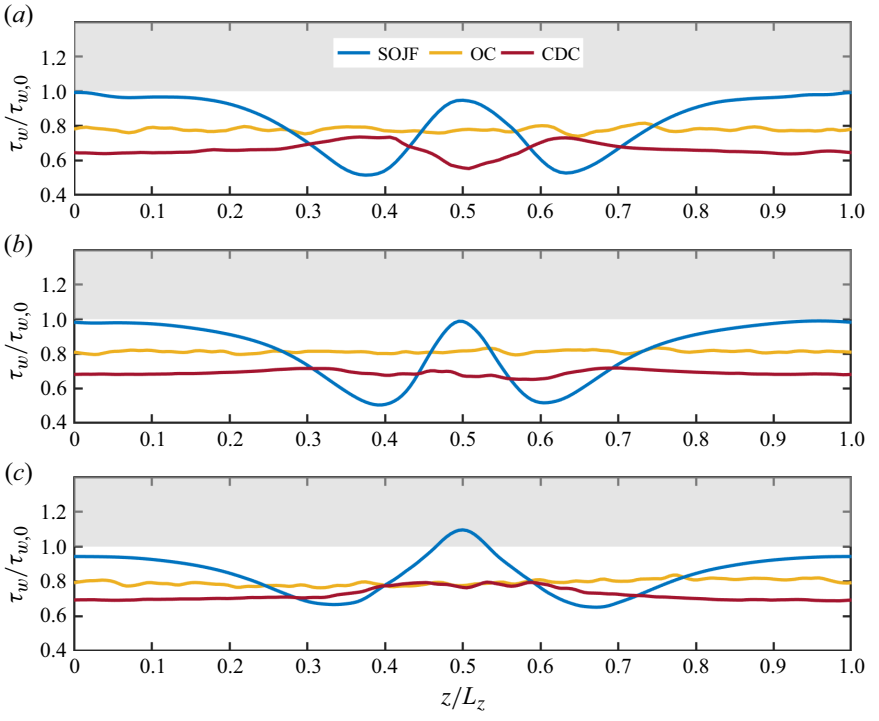


Figure 6. Spanwise variation of mean wall shear stress τ_w for SOJF (blue), OC (yellow), and CDC (red) normalised by uncontrolled wall stress at (*a*) $Re_\tau = 180$, (*b*) 395 and (*c*) 550.

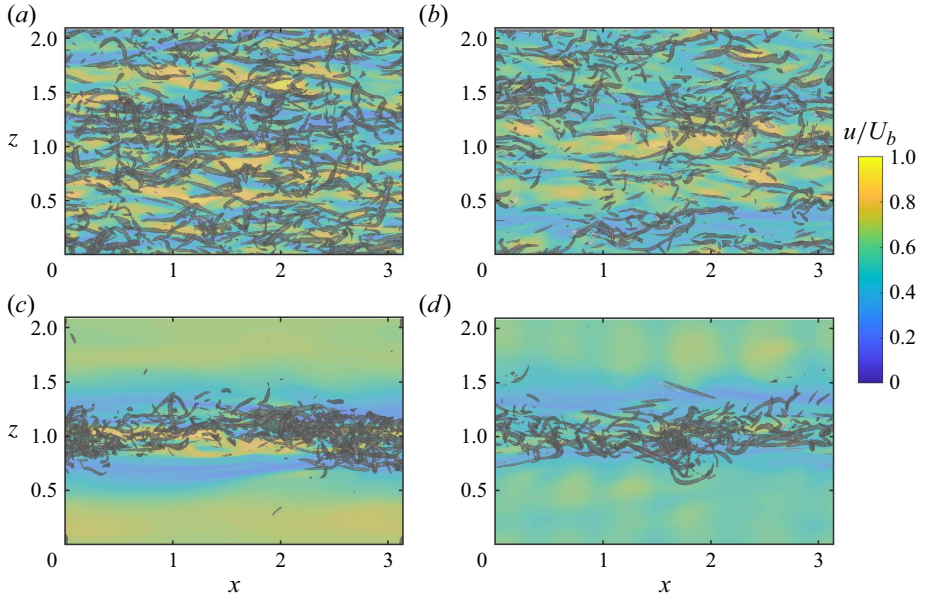


Figure 7. The λ_2 vortical structures plotted against the background of streamwise velocity contours in the plane of $y^+ = 15$ for flow with (*a*) no control, (*b*) OC, (*c*) SOJF and (*d*) CDC at $Re_\tau = 550$.

https://doi.org/10.1017/jfm.2026.12120 Published online by Cambridge University Press

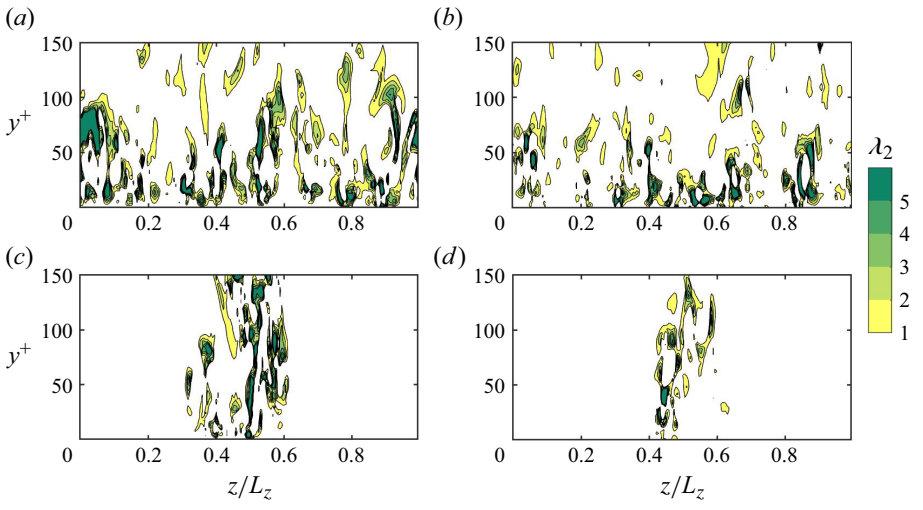


Figure 8. Cross-view of λ_2 vortical structures with (*a*) no control, (*b*) OC, (*c*) SOJF and (*d*) CDC at $Re_\tau = 550$.

and the strength of the λ_2 structures are suppressed under CDC, resulting in the greatest reduction in drag.

Compared with § 3.1 that focuses on the wall-normal variation, the plots here reveal more information on the horizontal plane with a connection to the vortical structures. However, since there are multiple scales of structures in the flow, it is natural to wonder about the characteristics of the scale property for these control strategies. This is discussed now.

4. Spectrum analysis and proper orthogonal decomposition

Despite the above explanations of drag variation, where the effect of CDC can apparently be traced to OC or SOJF, in figure 9 we find a surprising phenomenon that is not observed in either of the individual control methods. For uncontrolled flow (figure 9*a*), there are strips of intensive wall shear stress (with the mean subtracted) along the streamwise direction; for OC (figure 9*b*), the stress fluctuations are more intense due to the random nature of blowing and suction; for SOJF (figure 9*c*), the strips are located in the middle span under the convection of large-scale swirls. All these cases are similar to the velocity streak distributions in figure 7. However, the wall shear stress of CDC exhibits distinct belt structures on the two sides of the channel (figure 9*d*), which alternate periodically along the streamwise direction. As neither the large-scale swirls nor the OC introduce streamwise variations, the streamwise belt structures are fully unanticipated.

4.1. *Spectrum of wall shear stress*

For quantitative features of figure 9, the pre-multiplied spectrum of wall shear stress is displayed in figure 10. For flow without control, the spectrum is larger at lower wavenumbers, consistent with the long streaks in figure 9(*a*). For SOJF, the spectrum takes its maximum at the smallest k_x^+, in accordance with the merged streaks along the central region. For CDC, all Reynolds number cases show a robust peak at $k_x^+ \approx 0.026$, which corresponds to a prominent streamwise periodicity of $\lambda_x^+ \approx 240$ and explains the streamwise pattern observed in figure 9(*d*). As there is no spectrum peak under SOJF, the peak of CDC must be a consequence of the wall-normal excitations. Indeed, OC shows a spectrum maximum at $k_x^+ \approx 0.02$ in figure 10. However, the peak of OC is not

https://doi.org/10.1017/jfm.2026.12120 Published online by Cambridge University Press

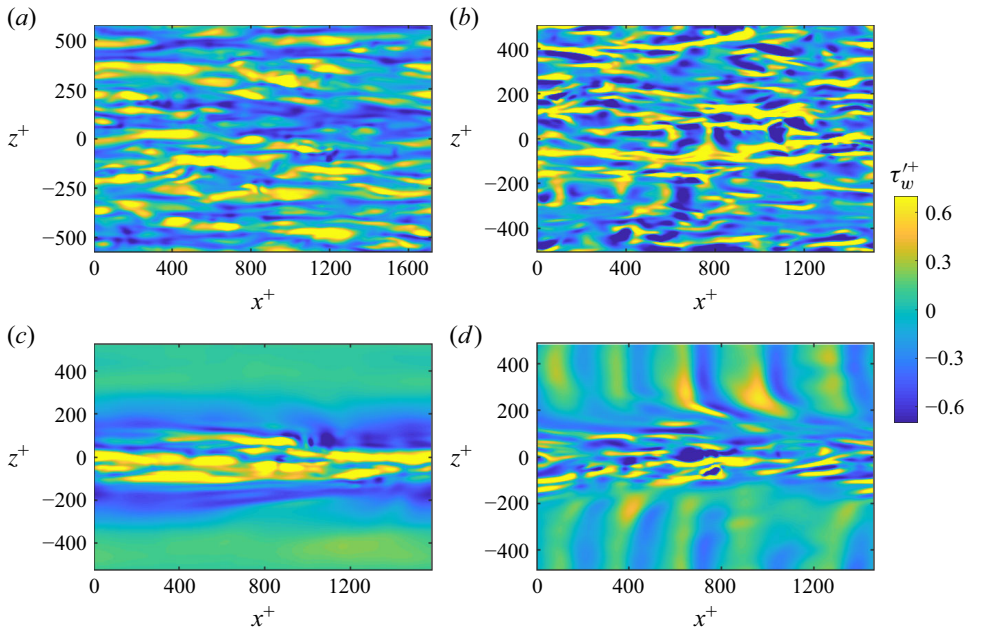


Figure 9. Contours of streamwise wall stress fluctuations for flow with (*a*) no control, (*b*) OC, (*c*) SOJF and (*d*) CDC at $Re_\tau = 550$.

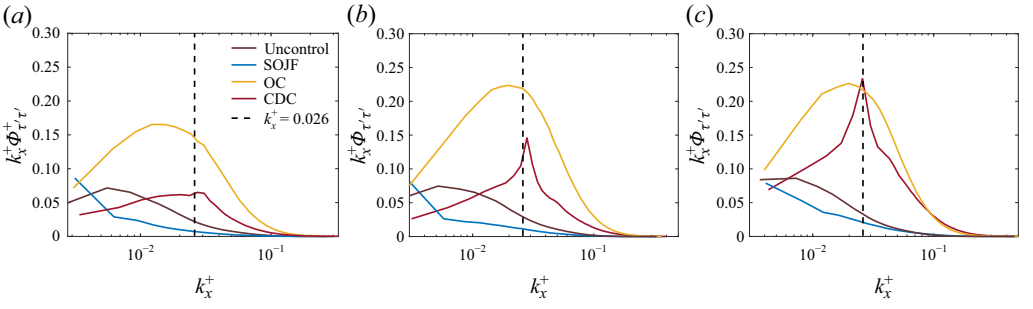


Figure 10. Pre-multiplied spectra of the wall stress fluctuations in the streamwise direction for (*a*) $Re_\tau = 180$, (*b*) $Re_\tau = 395$ and (*c*) $Re_\tau = 550$. The dashed line $k_x^+ = 0.026$ marks the spectrum peak of CDC, which corresponds to the wall stress belts in figure 9(*d*).

sharp, because of the wide range of activated fluctuating modes, therefore there is no clear periodicity in figure 9(*b*).

To confirm that the origin of the wall stress periodicity of CDC is related to the wall-normal motion rather than large-scale swirls, a further examination of the instantaneous velocity field is presented. Figure 11 shows the velocity contours in the viscous sublayer plane ($y^+ = 5$), the detection plane ($y^+ = 15$) and the buffer layer plane ($y^+ = 25$). For all velocity components, the wall-normal velocity v (figure 11*a–c*) shows the most distinctive periodicity in the horizontal planes, which highly resembles the characteristic of the wall shear stress (figure 9*d*). In contrast, there is barely any streamwise periodicity for the spanwise velocity w (figure 11*d–f*). For the streamwise velocity u, figure 11(*g*) shows clear periodic belts at $y^+ = 5$; with increasing y^+, the belts become blurred at $y^+ = 15$ (figure 11*h*) and even disappear at $y^+ = 25$ (figure 11*i*). This blurring with increasing y^+

https://doi.org/10.1017/jfm.2026.12120 Published online by Cambridge University Press

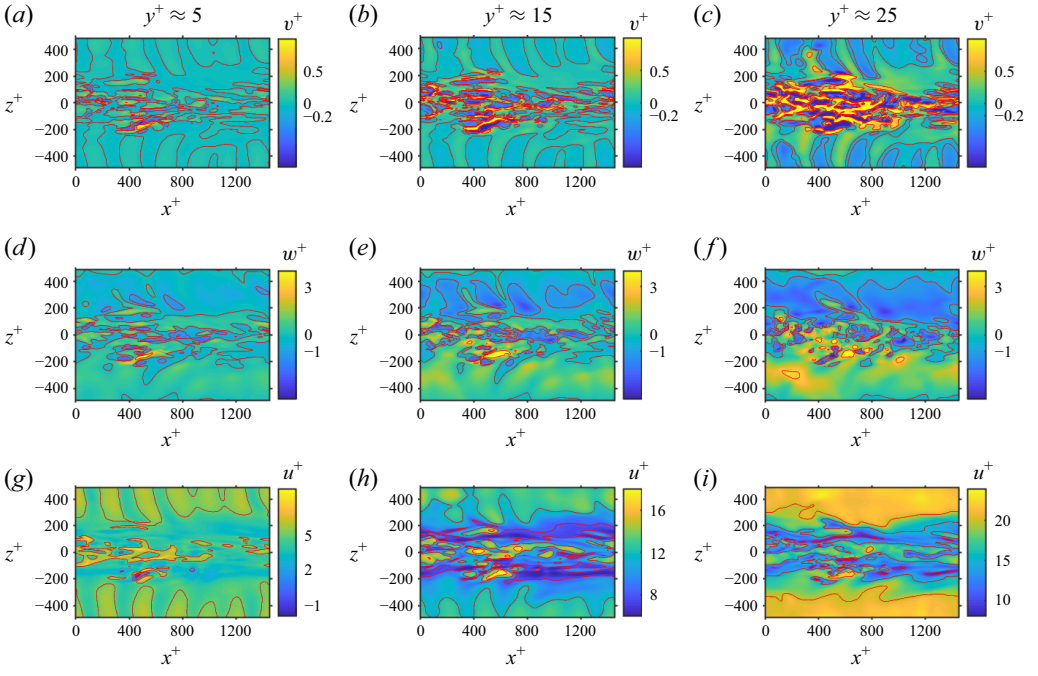


Figure 11. Slices of instantaneous velocity contours of CDC550 in the horizontal planes at $y^+ = 5$ (*a*,*d*,*g*), $y^+ = 15$ (*b*,*e*,*h*) and $y^+ = 25$ (*c*,*f*,*i*) for v^+ (*a*–*c*), w^+ (*d*–*f*) and u^+ (*g*–*i*). Here $z^+ = 0$ indicates the mid-span of a channel.

is understandable, because OC is active below the detection plane ($y^+ < 15$), while the flow is dominated by SOJF above the detection plane ($y^+ > 15$). Therefore, it is clear that the blowing and suction of the OC induce the streamwise periodicity.

4.2. *Proper orthogonal decomposition of velocity fields*

For the dynamic property of the belt structures, POD (Lumley 1967; Meyer *et al.* 2007) is applied to analyse the time dependence of the fluctuating velocity fields (for details, see Appendix A). Here, 1000 snapshots of the instantaneous streamwise velocity u and the wall-normal velocity v in the x–z plane at $y^+ \approx 5$ are collected, with a time interval of $\delta t = 0.003h/u_\tau$ (or $\delta t^+ \approx 1.45\nu/u_\tau^2$ in viscous time). The POD modes are then calculated separately for the velocity fluctuation of u' and v' after Reynolds decomposition, following a similar procedure to that for wake flows and turbulent boundary layers (Bergmann *et al.* 2005; Feng *et al.* 2011; Borra & Saxton-Fox 2022; Zhang *et al.* 2023; Borra *et al.* 2025).

Particularly for u', the first mode (figure 12*a*) shows very long streaks in the mid-span, while the second (figure 12*b*) and third (figure 12*c*) modes display streamwise belt structures on the two channel sides. Note that the first POD mode is different from the Fourier modes because the CDC breaks the translational invariance in the spanwise domain. However, translational invariance in the streamwise direction is preserved under CDC. Consequently, a travelling-wave structure (like Fourier modes) can still be identified in the second and third POD modes. It should be noted that the second and third modes form a degenerate pair, since they possess identical energy (about 7 % of total energy) but differ in phase by approximately $\pi/2$.

For v', the first two modes (figure 12*d*,*e*) show long strips along the mid-span, and the third mode (figure 12*f*) shows the belt structures. In Appendix A, we further show that the

https://doi.org/10.1017/jfm.2026.12120 Published online by Cambridge University Press

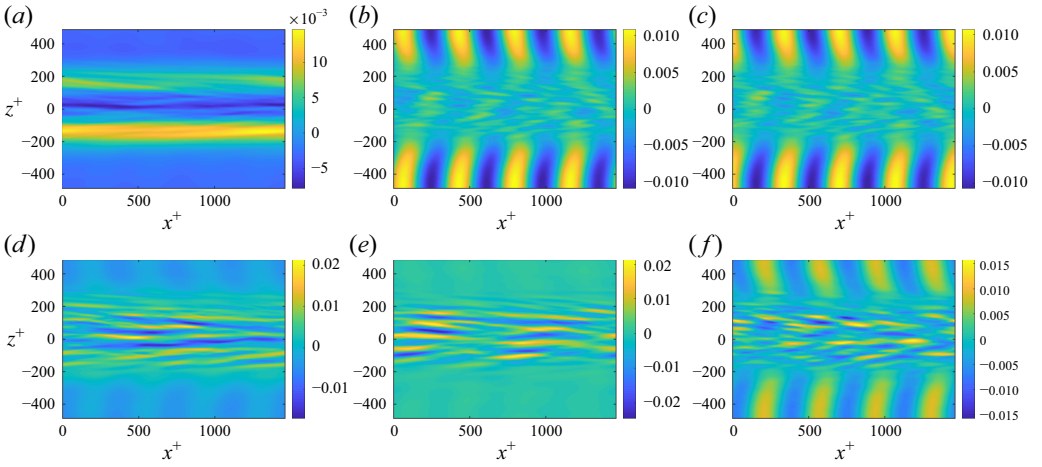


Figure 12. The POD modes of velocity fluctuations under CDC in the x–z plane of $y^+ = 5$ at $Re_\tau = 550$. (a–c) Modes 1–3 of streamwise velocity fluctuation; (d–f) modes 1–3 of vertical velocity fluctuation.

power spectral densities of these POD modes exhibit their peaks at the same time period of $T^+ \approx 30$ for both u' and v', hence indicating a robust dynamical feature scaled in viscous units, consistent with the periodicity of $\lambda_x^+ \approx 240$ scaled in viscous units as well. Note that the pattern observed in figure 12 resembles the subharmonic varicose mode, which is more stable than the sinuous instability mode (Andersson *et al.* 2001). Thus, we infer that under the composite control, the sinuous instability is suppressed due to a larger flank angle of the merged streak envelope – a mechanism illustrated in Schoppa & Hussain (2002) – whereas the subharmonic varicose waves survive and are strengthened by OC. This view awaits future verification.

5. Vortical decomposition of skin friction

In this section a vortical decomposition is performed to understand the Re_τ dependence of drag reduction. Through the Taylor vorticity equation, Chin *et al.* (2014), Yoon *et al.* (2016) and Zhao *et al.* (2024) have obtained a vortical decomposition of skin friction for flow without control. For controlled flow, Ji *et al.* (2021) derived

$$C_f = \underbrace{\int_0^2 \frac{\epsilon_M}{\epsilon_*}\,\mathrm{d}y'}_{C_\Omega} + \underbrace{\int_0^2 \frac{\overline{-v'\omega_z'}(\bar{u})}{\epsilon_*}\,\mathrm{d}y'}_{T_Z} + \underbrace{\int_0^2 \frac{\overline{w'\omega_y'}(\bar{u})}{\epsilon_*}\,\mathrm{d}y'}_{T_Y}, \tag{5.1}$$

where $\epsilon_* = U_b^3/h$ is the scale of the volume dissipation rate; C_Ω is the mean dissipation ($\epsilon_M = \nu \partial_y \bar{u} \partial_y \bar{u}$) induced by spanwise vorticity; T_Z is the wall-normal transport or dispersion of the spanwise vorticity; and T_Y is the spanwise dispersion of the wall-normal vorticity. As the mean velocity $\bar{u}$ in the integration breaks the Galilean invariance, (5.1) is only applicable to a static reference frame. For an inertial reference frame moving at any constant velocity U_m, (5.1) becomes valid by replacing $\bar{u}$ with $\bar{u} - U_m$. In addition, the sum of $T_Y + T_z$ exhibits Galilean invariance because C_f and C_Ω are independent of U_m. According to the triple decomposition, T_Z and T_Y can further be decomposed into

$$T_Z = T_{Z-R} + T_{Z-C}, \quad T_Y = T_{Y-R} + T_{Y-C}, \tag{5.2}$$

https://doi.org/10.1017/jfm.2026.12120 Published online by Cambridge University Press

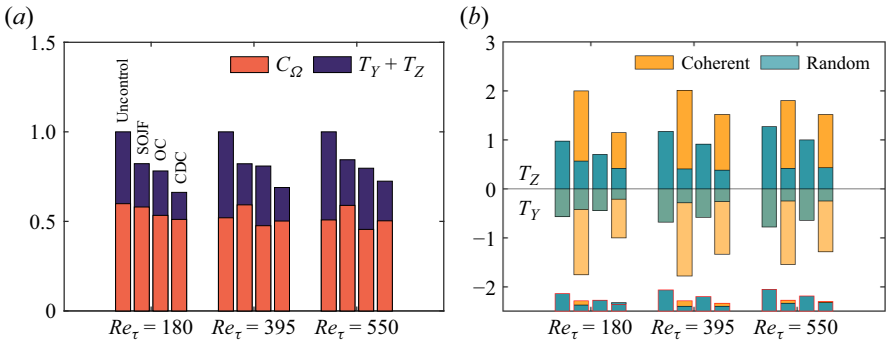


Figure 13. (*a*) Bar charts of C_Ω, $T_Z + T_Y$ in (5.1) for uncontrolled and controlled cases. (*b*) Bar charts of T_{Z-R}, T_{Z-C}, T_{Y-R}, T_{Y-C} and their sum (using the bottom as baseline) in (5.2) for uncontrolled and controlled cases. All components are normalised by $C_{f,0}$ without control.

where T_{Z-R} and T_{Y-R} are contributed by random dispersion, given respectively by $\overline{-v''\omega_z''}(\bar{u})/\epsilon_*$ and $\overline{w''\omega_y''}(\bar{u})/\epsilon_*$; T_{Z-C} and T_{Y-C} are contributed by coherent dispersion, given respectively by $\overline{-\tilde{v}\tilde{\omega}_z}(\bar{u})/\epsilon_*$ and $\overline{\tilde{w}\tilde{\omega}_y}(\bar{u})/\epsilon_*$.

Figure 13(*a*) presents bar charts of the mean vorticity dissipation C_Ω and the vortex dispersion $T_Y + T_Z$ under various controls and at different Re_τ. Compared with uncontrolled flow, SOJF reduces vortex dispersion by 16 % at $Re_\tau = 180$, by 24 % at $Re_\tau = 395$ and by 23 % at $Re_\tau = 550$, but with the disadvantage of enhancing the mean dissipation of vorticity with increasing Re_τ. For OC, the vortex dispersion is reduced by approximately 5 % and the mean dissipation by approximately 15 % for all Re_τ, resulting in a drag reduction of 20 % in total. For CDC, the vortex dispersion is reduced by 25 %, 29 % and 27 % for $Re_\tau = 180$, 395 and 550, respectively. However, the suppression of mean dissipation by CDC decreases from 9 % at $Re_\tau = 180$ to 1 % at $Re_\tau = 550$, indicating a decreasing contribution from control of mean vortical dissipation.

Bar charts showing random and coherent parts of T_Z and T_Y are further presented in figure 13(*b*) with the combined $T_Z + T_Y$ at bottom. In the upper part of figure 13(*b*), T_{Z-R} and T_{Z-C} for all cases are positively distributed, while the corresponding T_{Y-R} and T_{Y-C} in the lower part are negatively distributed. Under control, random vortex dispersion is significantly suppressed, particularly for SOJF and CDC. At $Re_\tau = 550$, T_{Z-R} is reduced from 127 % for uncontrol to 42 % for SOJF, 43 % for CDC and 99 % for OC. Similarly, T_{Y-R} is increased from −78 % for uncontrol to −25 % for SOJF, −25 % for CDC and −65 % for OC. However, under large-scale control, substantial coherent vortex dispersion is also induced for SOJF and CDC. At $Re_\tau = 550$, T_{Z-C} reaches 138 % for SOJF and 108 % for CDC, and T_{Y-C} reaches −130 % for SOJF and −104 % for CDC, indicating that the large-scale controlled swirls under CDC are weaker than those under SOJF. Compared with the uncontrolled case and OC, SOJF and CDC exhibit a weaker Reynolds-number dependence of random vortex dispersion. For instance, under CDC at $Re_\tau = 180$, 395 and 550, the corresponding T_{Z-R} values are 42 %, 37 % and 43 %, respectively, and the corresponding T_{Y-R} values are −22 %, −26 % and −25 %, respectively. These results suggest that random vortex motions are almost completely suppressed under CDC. Although random vortex dispersion is significantly reduced for SOJF and CDC, it is $T_Z + T_Y$ that provides the net contribution to the skin-friction coefficient. As shown by the bars with red edges at the bottom of figure 13(*b*), $T_{Z-R} + T_{Y-R}$ remains the dominant contributor to skin-friction drag, whereas $T_{Z-C} + T_{Y-C}$ is comparatively smaller. In particular, under CDC, T_{Z-C} is largely counterbalanced by T_{Y-C}, resulting in no net

https://doi.org/10.1017/jfm.2026.12120 Published online by Cambridge University Press

contribution to skin friction. Indeed, at $Re_\tau = 180$, $T_{Z-C} + T_{Y-C}$ even yields a negative net contribution to the skin-friction coefficient. These findings indicate that, under CDC, the role of large-scale controlled swirls is to stabilise the outer-layer flow without generating turbulent structures that transport momentum in the wall-normal direction.

To more clearly illustrate the modulation of the vortex dispersion fluxes by CDC, figure 14 presents profiles of fluxes related to T_Z (figure 14*a*,*c*,*e*,*g*) and T_Y (figure 14*b*,*d*,*f*,*h*) under different control strategies. For the uncontrolled case and OC alone, where no large-scale coherent swirls exist, the total flux (black line) coincides with the random turbulent flux (red line). Over most of the profiles, the vorticity dispersion in the y direction is positive, while the spanwise vorticity dispersion flux is negative, consistent with their integrated contributions T_Z and T_Y. In the uncontrolled case, the peak intensity of the vorticity dispersion fluxes occurs at $y^+ \approx 10$ to 20, corresponding to the region of streak formation. Under OC, the profiles exhibit minor changes for $y^+ < 10$, with the main effect being a marked reduction in the peak flux intensities (figure 14*e*,*f*), reflecting the suppression of streak formation by wall blowing/suction. The solid red lines in figures 14(*c*,*d*) and 14(*g*,*h*) demonstrate that SOJF significantly attenuates the random component of the vortex dispersion, and completely eliminates the T_{Z-R} components for $y^+ > 100$ and the T_{Y-R} components for $y^+ > 70$. Compared with SOJF alone, CDC yields a weaker coherent vortex dispersion profile with the peak location shifted to a higher wall-normal position at $y^+ \approx 50$ (figure 14*g*,*h*). It is worth noting that for $y^+ > 200$, the T_{Y-C} component vanishes, while the T_{Z-C} component does not; the latter is primarily contributed by large-scale coherent swirl structures. Note that the sign of T_{Z-C} in Ji *et al.* (2021) has been updated here under CDC. These graphs indicate that T_Z should be suppressed for a net drag reduction at higher values of Re_τ, with particular emphasis on T_{Z-C}.

As Re_τ increases, the mean dissipation loses its status as the leading-order contribution to C_f (Wei 2018; Chen *et al.* 2021). Thus, more effort should be devoted to eliminating the vortical dispersions of T_Z and T_Y. Figure 14 has validated that CDC strongly suppresses the random vortex dispersion across whole flow domain, especially at outer region, random vortex dispersion being totally eliminated. If this ability of CDC persists at higher Re_τ, it is expected that the canonical inertial-layer vortical dynamics would be altered significantly, and uniform momentum zones that yields high wall skin friction would be suppressed as well under CDC. If so, the portion of skin-friction drag originating from outer-region vortical structures would be mainly contributed by the large-scale swirls excited by SOJF. In addition, Yao *et al.* (2025) show that OC achieves nearly 18 % drag reduction at $Re_\tau = 2000$ in channel flow. Given that CDC combines the effects of OC and SOJF, it is expected that CDC can maintain a drag reduction level above 18 % at $Re_\tau = 2000$. However, it should be noted that it still remains as a challenge to implement CDC at high Re_τ, particularly regarding the design of actuators to generate the prescribed large-scale swirls and the sensing of wall-normal velocity in the diagnostic plane. The increased coherence of the near-wall flow induced by the large-scale swirls may facilitate the practical implementation of OC, which deserves future studies.

6. Conclusions

Through DNS of incompressible channel flows, this study systematically investigates the drag reduction performance of CDC that combines OC and SOJF at $Re_\tau = 180$, 395, 550. To identify the optimal parameters in the y_c^+ and A_S^+ planes, 114 CDC simulations were performed, and a significant drag reduction of $R > 28$ % was obtained for all Re_τ cases, much higher than that achieved by individual control using OC or SOJF. As the required

https://doi.org/10.1017/jfm.2026.12120 Published online by Cambridge University Press

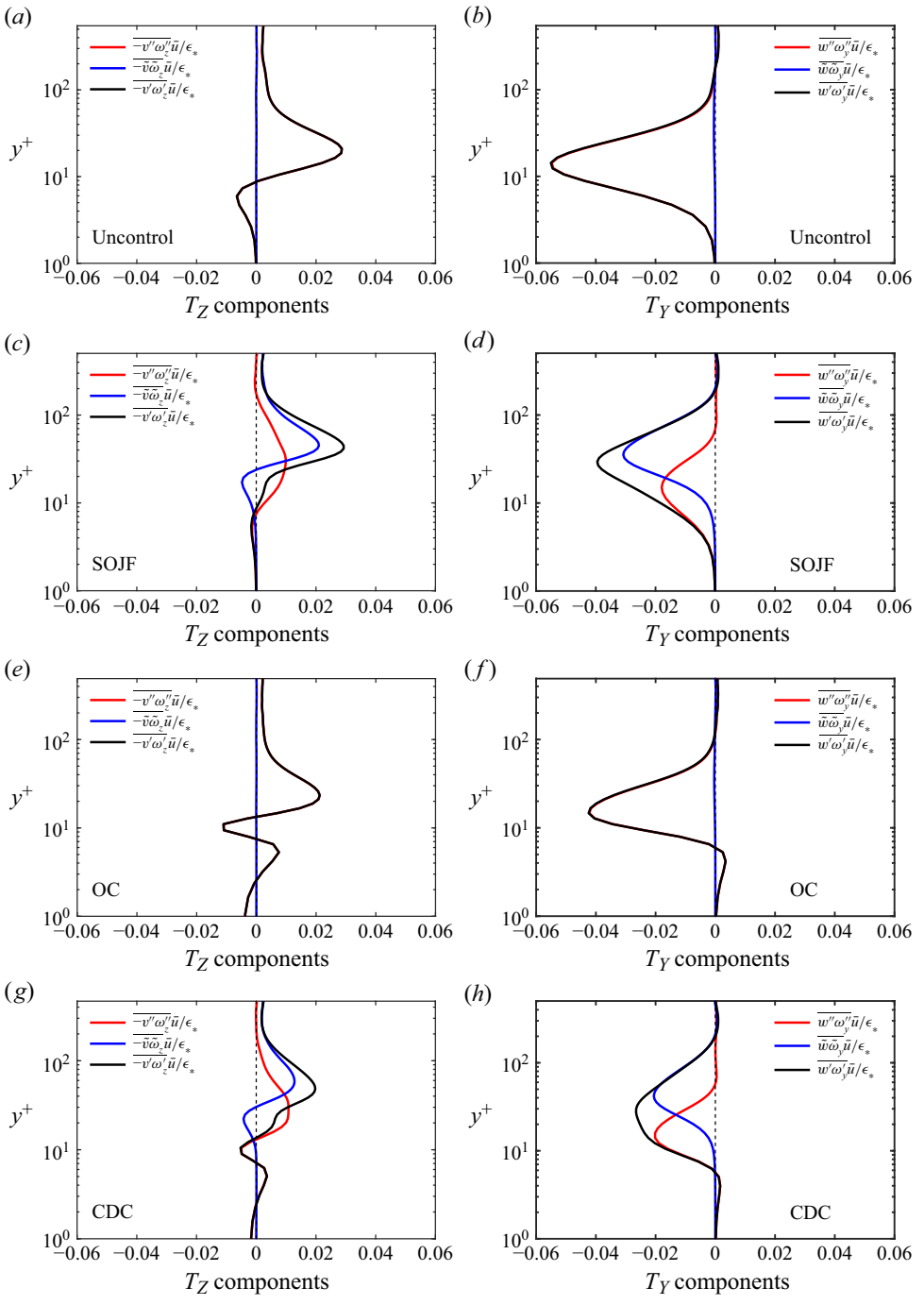


Figure 14. Wall-normal profiles of vorticity dispersion in the y direction (a,c,e,g) and z direction (b,d,f,h) for uncontrol (a,b), SOJF (c,d), OC (e,f) and CDC (g,h). Coherent, random and Reynolds-averaged components are represented by different colours, as marked in the legends.

https://doi.org/10.1017/jfm.2026.12120 Published online by Cambridge University Press

energy input of the CDC is less than 2 %, at least 26 % net power saving is achieved. Flow statistics show that CDC combines the advantages of OC and SOJF, effectively suppressing random turbulence in the inner and outer regions simultaneously.

Although the large-scale swirls induced by CDC are similar to those of SOJF, the mean wall shear stress of CDC is more homogeneous in the spanwise direction. Also, streamwise periodic belts are observed under CDC, and the pre-multiplied spectra show a sharp peak at the Re_τ-invariant wavenumber $k_x^+ \approx 0.026$. Analysis of velocity contours indicates that the streamwise periodicity is caused by the wall-normal motions of blowing and suction, whose characteristic length is $\lambda_x^+ \approx 240$. The streamwise periodic structures of CDC were confirmed using POD analysis, where the dynamic period was found to be $T^+ \approx 30$ in the viscous time scale. Finally, the vortical decomposition of C_f showed that eliminating the influence of the wall-normal vortical dispersion is essential to reduce drag as Re_τ increases. Future studies will explore the efficacy of CDC at even higher Re_τ and under different flow geometries.

Funding. X.C. acknowledges the support of the National Natural Science Foundation of China (grant no. 92252201) and the Fundamental Research Funds for the Central Universities.

Declaration of interests. The authors report no conflict of interest.

Data availability statement. The data that support the findings of this study are available from the corresponding author upon reasonable request.

Appendix A. Proper orthogonal decomposition analysis

Following Meyer *et al.* (2007) and Borra *et al.* (2025), the POD analysis was performed as follows. The snapshot $\boldsymbol{u} = u'(x, z)$ was rearranged as an $I = N_x \times N_z$ column vector. We collect $N = 1000$ such snapshots in time intervals of $0.003h/u_\tau$ and construct the matrix $\boldsymbol{U}$ as follows:

$$\boldsymbol{U} = \begin{bmatrix} \boldsymbol{u'}^1 & \boldsymbol{u'}^2 & \cdots & \boldsymbol{u'}^N \end{bmatrix} = \begin{bmatrix} u_1'^1 & u_1'^2 & \cdots & u_1'^N \\ \vdots & \vdots & \vdots & \vdots \\ u_I'^1 & u_I'^2 & \cdots & u_I'^N \end{bmatrix}. \tag{A1}$$

The superscript $j = 1, 2, \ldots, N$ indicates the number index of the snapshot. The objective of POD analysis is to find a hierarchical set of orthogonal modes to construct $\boldsymbol{U}$. To accomplish this goal, the autocovariance matrix was created as

$$\widetilde{\boldsymbol{M}} = \boldsymbol{U}^T \boldsymbol{U}, \tag{A2}$$

and then the eigenvalue problem for $\widetilde{\boldsymbol{M}}$, i.e.

$$\widetilde{\boldsymbol{M}} \boldsymbol{V}^j = \lambda^j \boldsymbol{V}^j, \tag{A3}$$

was solved. As the kinetic energy of a POD mode is proportional to the magnitude of its eigenvalue, the eigenvalues were rearranged from largest to smallest, that is,

$$\lambda^1 > \lambda^2 > \lambda^3 > \cdots > \lambda^N. \tag{A4}$$

Next, the normalised POD modes $\boldsymbol{\phi}^j$ were constructed using the eigenvectors given by (A3), i.e.

$$\boldsymbol{\phi}^j = \frac{\sum_{n=1}^N V_n^j \boldsymbol{u'}^n}{|| \sum_{n=1}^N V_n^j \boldsymbol{u'}^n ||}, \qquad j = 1, 2, 3, \ldots, N, \tag{A5}$$

https://doi.org/10.1017/jfm.2026.12120 Published online by Cambridge University Press

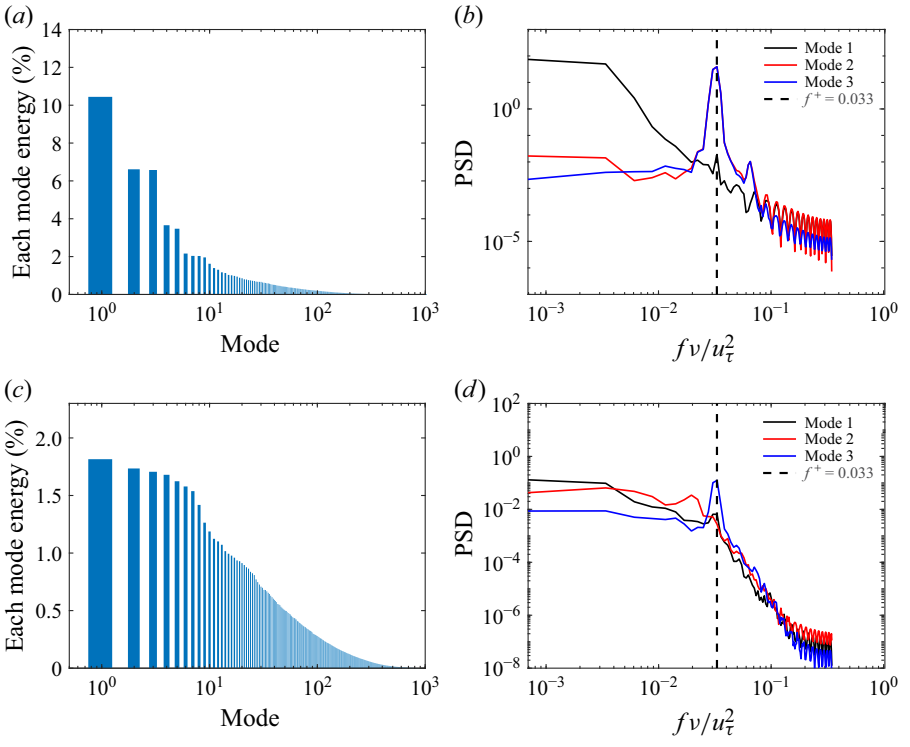


Figure 15. Energy proportion of each POD mode: (*a*) streamwise velocity fluctuation u'; (*c*) wall-normal velocity fluctuation v'. Power spectral density (PSD) of the first three POD expanded coefficients: (*b*) for u' and (*d*) for v'. Dashed lines in (*b*,*d*) mark the normalised frequency by the viscous time scale, i.e. $f^+ = 0.033$, where u'-modes 2 and 3 and v'-mode 3 have their peaks.

where V_n^j is the nth component of the eigenvector $\boldsymbol{V}^j$ with eigenvalue λ^j, and $||\boldsymbol{y}|| = \sqrt{y_1^2 + y_2^2 + y_3^2 + \cdots + y_I^2}$ is the L_2 norm of the vector $\boldsymbol{y}$. Because $\boldsymbol{\phi}^j$ form a complete orthogonal basis, $\boldsymbol{u'^n}$ can be expanded based on POD modes:

$$\boldsymbol{u'}^n = \sum_{i=1}^{N} c_j^n \boldsymbol{\phi}^j = \boldsymbol{\Phi} \boldsymbol{c}^n \tag{A6}$$

and the corresponding coefficients $\boldsymbol{c}^n$ are

$$\boldsymbol{c}^n = \boldsymbol{\Phi}^T \boldsymbol{u'}^n, \tag{A7}$$

where $\boldsymbol{\Phi} = [\boldsymbol{\phi}^1 \quad \boldsymbol{\phi}^2 \quad \boldsymbol{\phi}^3 \cdots \boldsymbol{\phi}^N]$.

The percentage of kinetic energy contained in each mode was calculated as $\lambda_i / \sum_{n=1}^{N} \lambda_n$, as shown in figure 15(*a*) for $\boldsymbol{u'}$. Mode 1 contributes about 11 % to the total kinetic energy, while modes 2 and 3 contribute similar amounts of 7 %; the remaining modes each contribute less than 4 % to the total kinetic energy. The power spectral densities of the temporal coefficients $\boldsymbol{c}^n$ for the first three modes ($n = 1, 2, 3$) are shown in figure 15(*b*). The first mode corresponds to the merged streak envelope (figure 12*a*), and the second and third modes correspond to the streamwise belt structures (figure 12*b*,*c*), both taking a maximum at a frequency of $f^+ = 0.033$. The latter indicates a viscous time scale of $T^+ = 1/f^+ \approx 30$ for the dynamical period of the belt structures.

https://doi.org/10.1017/jfm.2026.12120 Published online by Cambridge University Press

Similar POD analysis was performed for $\boldsymbol{v}'$, as shown in figure 15(c) for the energy contribution and figure 15(d) for the power spectral density. The first seven modes of v' make similar contributions to the total kinetic energy, each less than 2 %. The power spectral density of mode 3 exhibits a peak at a frequency of $f^+ = 0.033$, indicating the same period of $30\nu/u_\tau^2$ as for u'. This coincidence indicates that all the belt structures observed in figures 12(b), 12(c) and 12(f) have the same dynamical property.

References

Agostini, L., Touber, E. & Leschziner, M.A. 2014 Spanwise oscillatory wall motion in channel flow: drag-reduction mechanisms inferred from DNS-predicted phase-wise property variations at *Re* 1000. *J. Fluid Mech.* **743**, 606–635.

Andersson, P., BrandtT, L., Bottaro, A. & Henningson, D.S. 2001 On the breakdown of boundary layer streaks. *J. Fluid Mech.* **428**, 29–60.

Bechert, D.W., Bruse, M., Hage, W., Van der Hoeven, J.G.T. & Hoppe, G. 1997 Experiments on drag-reducing surfaces and their optimization with an adjustable geometry. *J. Fluid Mech.* **338**, 59–87.

Bergmann, M., Cordier, L. & Brancher, J.-P. 2005 Optimal rotary control of the cylinder wake using proper orthogonal decomposition reduced-order model. *Phys. Fluids* **17** (9), 097101.

Borra, A., Flynn, Z., Goza, A. & Saxton-Fox, T. 2025 Intrinsic phase-based proper orthogonal decomposition: a method for physically interpretable modes in near-periodic systems. *J. Fluid Mech.* **1002**, A18.

Borra, A. & Saxton-Fox, T. 2022 Proper orthogonal decomposition for a turbulent boundary layer with aero-optic distortion. *AIAA J.* **60** (6), 3555–3564.

Cannata, M., Cafiero, G. & Iuso, G. 2020 Large-scale forcing of a turbulent channel flow through spanwise synthetic jets. *AIAA J.* **58** (5), 2042–2052.

Canton, J., Örlü, R., Chin, C. & Schlatter, P. 2016 Reynolds number dependence of large-scale friction control in turbulent channel flow. *Phys. Rev. Fluids* **1** (8), 081501.

Chandran, D., Zampiron, A., Rouhi, A., Fu, M.K., Wine, D., Holloway, B., Smits, A.J. & Marusic, I. 2023 Turbulent drag reduction by spanwise wall forcing. Part 2. High-Reynolds-number experiments. *J. Fluid Mech.* **968**, A7.

Checco, A., Ocko, B.M., Rahman, A., Black, C.T., Tasinkevych, M., Giacomello, A. & Dietrich, S. 2014 Collapse and reversibility of the superhydrophobic state on nanotextured surfaces. *Phys. Rev. Lett.* **112** (21), 216101.

Chen, X., Hussain, F. & She, Z. 2019 Non-universal scaling transition of momentum cascade in wall turbulence. *J. Fluid Mech.* **871**, R2.

Chen, X., Yao, J. & Hussain, F. 2021 Theoretical framework for energy flux analysis of channels under drag control. *Phys. Rev. Fluids* **6**, 013902.

Cheng, X.Q., Wong, C.W., Hussain, F., Schröder, W. & Zhou, Y. 2021 Flat plate drag reduction using plasma-generated streamwise vortices. *J. Fluid Mech.* **918**, A24.

Chevalier, M., Schlatter, P., Lundbladh, A. & Henningson, D. 2007 SIMSON–A pseudo-spectral solver for incompressible boundary layer flow. *Tech. Rep*. TRITA-MEK 2007:07. Royal Institute of Technology.

Chin, C., Philip, J., Klewicki, J., Ooi, A. & Marusic, I. 2014 Reynolds-number-dependent turbulent inertia and onset of log region in pipe flows. *J. Fluid Mech.* **757**, 747–769.

Choi, H., Moin, P. & Kim, J. 1993 Direct numerical simulation of turbulent flow over riblets. *J. Fluid Mech.* **255**, 503–539.

Choi, H., Moin, P. & Kim, J. 1994 Active turbulence control for drag reduction in wall-bounded flows. *J. Fluid Mech.* **262**, 75–110.

Chung, D., Hutchins, N., Schultz, M.P. & Flack, K.A. 2021 Predicting the drag of rough surfaces. *Annu. Rev. Fluid Mech.* **53**, 439–471.

Chung, Y.M. & Talha, T. 2011 Effectiveness of active flow control for turbulent skin friction drag reduction. *Phys. Fluids* **23** (2), 025102.

Corke, T.C. & Thomas, F.O. 2018 Active and passive turbulent boundary-layer drag reduction. *AIAA J.* **56** (10), 3835–3847.

Del Alamo, J.C. & Jimenez, J. 2006 Linear energy amplification in turbulent channels. *J. Fluid Mech.* **559**, 205–213.

Deng, B.-Q. & Xu, C.-X. 2012 Influence of active control on STG-based generation of streamwise vortices in near-wall turbulence. *J. Fluid Mech.* **710**, 234–259.

https://doi.org/10.1017/jfm.2026.12120 Published online by Cambridge University Press

DENG, B.-Q., XU, C.-X., HUANG, W.-X. & CUI, G.-X. 2014 Strengthened opposition control for skin-friction reduction in wall-bounded turbulent flows. *J. Turbul.* **15** (2), 122–143.
DESHPANDE, R., CHANDRAN, D., SMITS, A.J. & MARUSIC, I. 2023 On the relationship between manipulated inter-scale phase and energy-efficient turbulent drag reduction. *J. Fluid Mech.* **972**, A12.
DESHPANDE, R., KIDANEMARIAM, A. & MARUSIC, I. 2024 Pressure drag reduction via imposition of spanwise wall oscillations on a rough wall. *J. Fluid Mech.* **979**, A21.
DUAN, P.-Y., CHEN, X., JI, Y., YAO, J. & HUSSAIN, F. 2024 Large-scale control in turbulent flows over surface riblets. *Phys. Fluids* **36**, 095137.
DUONG, A.H., CORKE, T.C. & THOMAS, F.O. 2021 Characteristics of drag-reduced turbulent boundary layers with pulsed-direct-current plasma actuation. *J. Fluid Mech.* **915**, A113.
FENG, L.-H., WANG, J.-J. & PAN, C. 2011 Proper orthogonal decomposition analysis of vortex dynamics of a circular cylinder under synthetic jet control. *Phys. Fluids* **23** (1), 014106.
FLORYAN, D. 2023 A fundamental limit on energy savings in controlled channel flow, and how to beat it. *J. Fluid Mech.* **954**, R3.
FUKAGATA, K., IWAMOTO, K. & HASEGAWA, Y. 2024 Turbulent drag reduction by streamwise traveling waves of wall-normal forcing. *Annu. Rev. Fluid Mech.* **56** (1), 69–90.
FUKAGATA, K., IWAMOTO, K. & KASAGI, N. 2002 Contribution of Reynolds stress distribution to the skin friction in wall-bounded flows. *Phys. Fluids* **14** (11), 73–76.
GATTI, D., CIMARELLI, A., HASEGAWA, Y., FROHNAPFEL, B. & QUADRIO, M. 2018 Global energy fluxes in turbulent channels with flow control. *J. Fluid Mech.* **857**, 345–373.
GATTI, D., VON DEYN, L.H., FOROOGHI, P. & FROHNAPFEL, B. 2020 Do riblets exhibit fully rough behaviour? *Exp. Fluids* **61**, 1–6.
GATTI, D. & QUADRIO, M. 2016 Reynolds-number dependence of turbulent skin-friction drag reduction induced by spanwise forcing. *J. Fluid Mech.* **802**, 553–582.
GATTI, D., QUADRIO, M., CHIARINI, A., GATTERE, F. & PIROZZOLI, S. 2025 Turbulent skin-friction drag reduction via spanwise forcing at high Reynolds number. *J. Fluid Mech.* **1016**, A58.
DE GIOVANETTI, M., HWANG, Y. & CHOI, H. 2016 Skin-friction generation by attached eddies in turbulent channel flow. *J. Fluid Mech.* **808**, 511–538.
GUSEVA, A. & JIMÉNEZ, J. 2022 Linear instability and resonance effects in large-scale opposition flow control. *J. Fluid Mech.* **935**, A35.
HAN, B.-Z. & HUANG, W.-X. 2020 Active control for drag reduction of turbulent channel flow based on convolutional neural networks. *Phys. Fluids* **32** (9), 095108.
HURST, E., YANG, Q. & CHUNG, Y.M. 2014 The effect of Reynolds number on turbulent drag reduction by streamwise travelling waves. *J. Fluid Mech.* **759**, 28–55.
IUSO, G., ONORATO, M., SPAZZINI, P.G. & DI CICCA, G.M. 2002 Wall turbulence manipulation by large-scale streamwise vortices. *J. Fluid Mech.* **473**, 23–58.
JEONG, J. & HUSSAIN, F. 1995 On the identification of a vortex. *J. Fluid Mech.* **285**, 69–94.
JEONG, J., HUSSAIN, F., SCHOPPA, W. & KIM, J. 1997 Coherent structures near the wall in a turbulent channel flow. *J. Fluid Mech.* **332**, 185–214.
JI, Y., YAO, J., HUSSAIN, F. & CHEN, X. 2021 Vorticity transports in turbulent channels under large-scale control via spanwise wall jet forcing. *Phys. Fluids* **33** (9), 095112.
JIMENEZ, J. 2004 Turbulent flows over rough walls. *Annu. Rev. Fluid Mech.* **36**, 173–196.
JIMENEZ, J. & HOYAS, S. 2008 Turbulent fluctuations above the buffer layer of wall-bounded flows. *J. Fluid Mech.* **611**, 215–236.
JIMÉNEZ, J. & PINELLI, A. 1999 The autonomous cycle of near-wall turbulence. *J. Fluid Mech.* **389**, 335–359.
JUNG, W.J., MANGIAVACCHI, N. & AKHAVAN, R. 1992 Suppression of turbulence in wall-bounded flows by high-frequency spanwise oscillations. *Phys. Fluids A: Fluid Dyn.* **4** (8), 1605–1607.
KAMETANI, Y. & FUKAGATA, K. 2011 Direct numerical simulation of spatially developing turbulent boundary layers with uniform blowing or suction. *J. Fluid Mech.* **681**, 154–172.
KIM, J. & BEWLEY, T.R. 2007 A linear systems approach to flow control. *Annu. Rev. Fluid Mech.* **39**, 383–417.
LI, W., FAN, Y.T., MODESTI, D. & CHENG, C. 2019 Decomposition of the mean skin-friction drag in compressible turbulent channel flows. *J. Fluid Mech.* **875**, 101–123.
LUMLEY, J.L. 1967 The structure of inhomogeneous turbulent flow. In *Atmospheric Turbulence and Radio Wave Propagation* (ed. A.M. Yaglom & V.I. Tatarski), pp. 166–178. Nauka.
LUNDBLADH, A., HENNINGSON, D.S. & JOHANSSON, A.V. 1992 An efficient spectral integration method for the solution of the Navier–Stokes equations. FFA-TN 1992-28. Aeronautical Research Institute of Sweden, Bromma.

https://doi.org/10.1017/jfm.2026.12120 Published online by Cambridge University Press

MAMORI, H., IWAMOTO, K. & MURATA, A. 2014 Effect of the parameters of traveling waves created by blowing and suction on the relaminarization phenomena in fully developed turbulent channel flow. *Phys. Fluids* **26** (1), 015101.
MARUSIC, I., CHANDRAN, D., ROUHI, A., FU, M., WINE, D., HOLLOWAY, B., CHUNG, D. & SMITS, A. 2021 An energy-efficient pathway to turbulent drag reduction. *Nat. Commun.* **12**, 5805.
MEYER, K.E., PEDERSEN, J.M. & ÖZCAN, O. 2007 A turbulent jet in crossflow analysed with proper orthogonal decomposition. *J. Fluid Mech.* **583**, 199–227.
MODESTI, D., ENDRIKAT, S., HUTCHINS, N. & CHUNG, D. 2021 Dispersive stresses in turbulent flow over riblets. *J. Fluid Mech.* **917**, A55.
NOZARIAN, S., ABKAR, M. & FOROOGHI, P. 2024 An analysis of drag reduction using spanwise forcing on rough walls. *Intl J. Heat Fluid Flow* **106**, 109306.
OLIVER, T.A., MALAYA, N., ULERICH, R. & MOSER, R.D. 2014 Estimating uncertainties in statistics computed from direct numerical simulation. *Phys. Fluids* **26** (3), 035101.
PARK, H., SUN, G. & KIM, C.J. 2014 Superhydrophobic turbulent drag reduction as a function of surface grating parameters. *J. Fluid Mech.* **747**, 722–734.
PARK, J. & CHOI, H. 2020 Machine-learning-based feedback control for drag reduction in a turbulent channel flow. *J. Fluid Mech.* **904**, A24.
QUADRIO, M., RICCO, P. & VIOTTI, C. 2009 Streamwise-travelling waves of spanwise wall velocity for turbulent drag reduction. *J. Fluid Mech.* **627**, 161–178.
RASTEGARI, A. & AKHAVAN, R. 2018 The common mechanism of turbulent skin-friction drag reduction with superhydrophobic longitudinal microgrooves and riblets. *J. Fluid Mech.* **838**, 68–104.
RENARD, N. & DECK, S. 2016 A theoretical decomposition of mean skin friction generation into physical phenomena across the boundary layer. *J. Fluid Mech.* **790**, 339–367.
RICCO, P., SKOTE, M. & LESCHZINER, M.A. 2021 A review of turbulent skin-friction drag reduction by near-wall transverse forcing. *Prog. Aerosp. Sci.* **123**, 100713.
ROCCON, A., ZONTA, F. & SOLDATI, A. 2021 Energy balance in lubricated drag-reduced turbulent channel flow. *J. Fluid Mech.* **911**, A37.
ROTHSTEIN, J.P. 2010 Slip on superhydrophobic surfaces. *Annu. Rev. Fluid Mech.* **42**, 89–109.
ROUHI, A., FU, M.K., CHANDRAN, D., ZAMPIRON, A., SMITS, A.J. & MARUSIC, I. 2023 Turbulent drag reduction by spanwise wall forcing. Part 1. Large-eddy simulations. *J. Fluid Mech.* **968**, A6.
SCHLATTER, P., LI, Q., BRETHOUWER, G., JOHANSSON, A.V. & HENNINGSON, D.S. 2010 Simulations of spatially evolving turbulent boundary layers up to $Re_{heta} = 4300$. *Intl J. Heat Fluid Flow* **31** (3), 251–261.
SCHOPPA, W. & HUSSAIN, F. 1998 A large-scale control strategy for drag reduction in turbulent boundary layers. *Phys. Fluids* **10** (5), 1049–1051.
SCHOPPA, W. & HUSSAIN, F. 2002 Coherent structure generation in near-wall turbulence. *J. Fluid Mech.* **453**, 57–108.
SUMITANI, Y. & KASAGI, N. 1995 Direct numerical simulation of turbulent transport with uniform wall injection and suction. *AIAA J.* **33** (7), 1220–1228.
THOMAS, F., CORKE, T., HUSSAIN, F., DUONG, A., MCGOWAN, R., JASINSKI, C. & SIMMONS, D. 2016 Turbulent boundary layer drag reduction by active control of streak transient growth. In *Bulletin of the APS, 69th Annual Meeting of the APS Division of Fluid Dynamics*, vol. 61. 20. American Physical Society.
WALEFFE, F. 1997 On a self-sustaining process in shear flows. *Phys. Fluids* **9** (4), 883–900.
WEI, T. 2018 Integral properties of turbulent-kinetic-energy production and dissipation in turbulent wall bounded flows. *J. Fluid Mech.* **854**, 449.
XIAO, M., CECI, A., ORLANDI, P. & PIROZZOLI, S. 2024 Direct numerical simulation of drag reduction in rotating pipe flow up to $Re_\tau \approx 3000$. *J. Fluid Mech.* **996**, A24.
YAKENO, A., HASEGAWA, Y. & KASAGI, N. 2014 Modification of quasi-streamwise vortical structure in a drag-reduced turbulent channel flow with spanwise wall oscillation. *Phys. Fluids* **26** (8), 085109.
YAO, J., CHEN, X. & HUSSAIN, F. 2018 Drag control in wall-bounded turbulent flows via spanwise opposed wall-jet forcing. *J. Fluid Mech.* **852**, 678–709.
YAO, J., CHEN, X. & HUSSAIN, F. 2021 Composite active drag control in turbulent channel flows. *Phys. Rev. Fluids* **6**, 054605.
YAO, J., GARCÍA, E. & HUSSAIN, F. 2025 Drag reduction via opposition control in turbulent channel flows at high Reynolds numbers. *Phys. Rev. Fluids* **10**, 094604.
YOON, M., AHN, J. & HWANG, J. 2016 Contribution of velocity-vorticity correlations to the frictional drag in wall-bounded turbulent flows. *Phys. Fluids* **28**, 081702.
YUDHISTIRA, I. & SKOTE, M. 2011 Direct numerical simulation of a turbulent boundary layer over an oscillating wall. *J. Turbul.* **12**, N9.

https://doi.org/10.1017/jfm.2026.12120 Published online by Cambridge University Press

ZHANG, W., YANG, X.I.A., CHEN, P. & WAN, M. 2024 Integral methods for friction decomposition and their extensions to rough-wall flows. *J. Fluid Mech.* **985**, A46.

ZHANG, Y., HODŽIĆ, A., EVRARD, F., VAN WACHEM, B. & VELTE, C.M. 2023 Phase proper orthogonal decomposition of non-stationary turbulent flow. *Phys. Fluids* **35** (4), 045109.

ZHAO, Y., FAN, Y. & LI, W. 2024 Reynolds number effects on a velocity–vorticity correlation-based skin-friction drag decomposition in incompressible turbulent channel flows. *J. Fluid Mech.* **979**, A20.

https://doi.org/10.1017/jfm.2026.12120 Published online by Cambridge University Press